Conference on Modelling Fluid Flow (CMFF'25)
The 19th International Conference on Fluid Flow Technologies
Budapest, Hungary, August 26-August 29, 2025

MODELING OF FACE MASK FLOW AND DROPLET FILTRATION

Shijie XU[2], Leilei XU[2], Róbert Z. SZÁSZ[1], Xue-Song BAI[2], I.A.Sofia LARSSON[3], Per GREN[3], Mikael SJÖDAHL[3], Joel WAHL[3], Mihai MIHAESCU[4], Marco LAUDATO[4], Dario MAGGIOLO[5], Srdjan SASIC[5], T. Staffan LUNDSTRÖM[3]

[2] Department of Energy Sciences, Lund University, Lund, Sweden
[1] Corresponding Author. Department of Energy Sciences, Lund University, Sweden, E-mail: robert-zoltan.szasz@energy.lth.se
[3] Luleå University of Technology, Sweden
[4] KTH Royal Institute of Technology, Stockholm, Department of Engineering Mechanics, FLOW Research Center, Sweden
[5] Department of Mechanics and Maritime Sciences, Chalmers University of Technology, 412 96, Gothenburg, Sweden.

ABSTRACT

This paper presents experimental and numerical investigations of liquid droplet/air two-phase flow through face masks. The study aims to provide a deeper understanding of the droplet filtration process, generate experimental data for modeling droplet/air two-phase flow across face masks, and develop and validate numerical models to simulate droplet motion through the mask and downstream. Droplet interception and collection in the mask are investigated by detailed lattice Boltzmann simulations. Experiments are conducted in a branching pipe rig to measure filtration efficiency and droplet distribution at the outlet. The numerical models are applied to predict droplet motion within the experimental setup, demonstrating good agreement in terms of droplet emissions. The model is further employed to simulate airflow and droplet behavior around a human face during coughing. The results reveal a significant reduction in flow velocity across the face mask and more than a 60% decrease in droplet penetration distance.

Keywords: LES, IPI, face mask, droplets, filtration

NOMENCLATURE

D	$[m^{-4}]$	Darcy coefficient
F	$[m^{-3}]$	Forchheimer coefficient
L	$[m]$	thickness
d	$[m]$	diameter
p	$[Pa]$	pressure
$\underline{u}$	$[m/s]$	velocity
η	$[-]$	filtration efficiency
μ	$[m]$	dynamic viscosity
ρ	$[kg/m^3]$	density
$\wp$	$[-]$	size distribution

1. INTRODUCTION

Among different measures, the use of face masks is a key component of preventive strategies to minimize the spread of respiratory diseases. Due to the large number of masks used in an potential future pandemic, it is imperative to reduce their environmental footprint while preserving their functionality and user comfort.

Disposable masks, such as surgical masks, N95-100 in the U.S., and FFP1-3 in Europe, pose a significant environmental burden. It is estimated that over 140 billion disposable masks were used globally per month during the early stages of the pandemic [1]. This burden encompasses everything from greenhouse gas emissions during production to landfilling and littering. The World Health Organization (WHO) recommends that disposable masks be discarded as municipal waste, preferably through incineration [2]. While this approach has both benefits and drawbacks, it is problematic that waste is often disposed of in open landfills, especially in developing countries with limited resources for proper waste management [3].

Additionally, the landfilling of mask waste generates microplastics, which are present in landfill leachates and subsequently released into the surrounding environment [4]. Recycling disposable masks is also a complex challenge, as it may require prior decontamination and specialized procedures for separating the various polymer types used in masks, which can then be repurposed, for example, as energy sources [5].

The environmental impact of face masks largely depends on their usage. For instance, the greenhouse gas emissions associated with producing simple cotton cloth masks and disposable surgical masks are comparable. Still, factors such as washing and transportation can shift the environmental balance in favor of either option [6].

Thus, future face masks need to be carefully designed to achieve the desired low environmental impact, ensure proper comfort, and avoid significant economic penalties. Due to the pandemic, a large amount of published research has focused on various aspects of face masks. Mittal et al. [7] gives a detailed overview of the relevant physical phenomena, as well as the experimental and numerical methods used in their investigation, identifying the droplet filtration model used in macroscale simulations as one of the key challenges for numerical simulations. The review article by Hu et al. [8] presents an overview of various experimental methods used to investigate the distribution of particle sizes and the airflow behaviors of human respiration, concluding that there is a need for better spatial and temporal resolution and better quantification of the impact of face coverings.

This paper reports the first steps to reach our overall goal of developing a state-of-the-art experimental and numerical platform connecting experimental investigations of filtration efficiencies, Lattice Boltzmann simulations of droplet interception in the mask material, and large-scale Computational Fluid Dynamics (CFD) simulations to study the impact of face masks in realistic scenarios. The paper presents a novel idea, inspired by the thickened flame (see, e.g., [9]) model, to alleviate issues due to large gradients in the mask region. Furthermore, we investigate the potential of using machine learning methods to incorporate pore-scale physics in large-scale CFD simulations efficiently.

2. METHODS

2.1. Experiments

In the experiments, the droplet distribution in the downstream proximity of the masks is quantified using two different interferometric techniques. The double-pulsed interferometric particle imaging (IPI) technique is used to measure droplets larger than approximately 5 μm. The basic principle of IPI is the generation of two dominant glare points when a monochromatic plane wave, such as a laser, illuminates a particle [10]. When the glare points are defocused, they overlap, producing a fringe pattern at the defocused spot. The number of fringes is proportional to the size of the observed particle. IPI measurements allow the determination of both the size and position of individual particles. By introducing double-pulsed registration, it is also possible to estimate velocities between two frames [11].

For smaller particles, down to a few tens of nanometers, the dual-view polarization-resolved holographic method is used [12]. Smaller droplets scatter light differently depending on the polarization of the illumination, meaning that the state of polarization of the scattered light can be used as a metric to determine the size of individual particles. Combined with double-pulsed holographic registration and reconstruction, this method enables detailed determination of 3D size distributions and velocities. The interferometric data serve as input and validation data for the numerical simulations.

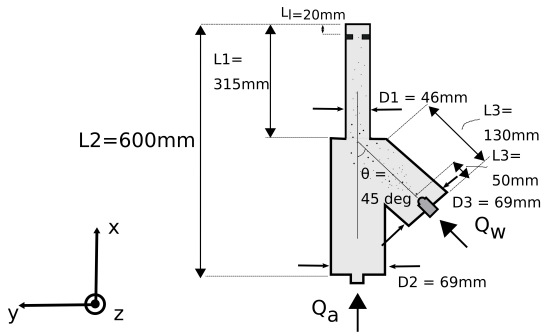

Figure 1. Experimental set-up. Air with flowrate Q_a enters through pipe 2 of diameter D2. Water is injected with a flow rate Q_w into pipe 3 with a diameter D3. The mask material is attached at the outlet of pipe 1 with diameter D1.

Figure 1 illustrates the experimental setup, which consists of three interconnected pipes. The first pipe, with a diameter of 69 mm, supplies air and connects to a second pipe of the same diameter at a 45-degree angle. Downstream of these branching pipes, a smaller pipe with a 46 mm diameter is attached. A face mask is mounted to the outlet. Various face masks are used in the experiments, including surgical masks, C-19 masks, synthetic cloth masks, and cotton cloth masks.

The experiments were conducted with or without leakage at the sides of the face mask. To control leakage, two slits perpendicular to the airflow are positioned 20 mm upstream of the face mask and can be toggled open or closed as needed.

Air with a constant speed of 1.62 m/s enters through the inlet denoted Q_a. Water droplets are injected into the upper branch of the geometry (Q_w) with a constant mass flow rate of 1.317×10^{-3} kg/s. More details about the experiments are given in [11].

2.2. Modeling of droplet dynamics in face mask

In this work, we employ two types of numerical studies: pore-scale high-fidelity simulations and Lagrangian Particle Tracking (LPT) of parcels representing saliva droplets. For the former, we carry out direct numerical simulations using a lattice Boltzmann framework to elucidate the effects of fibrous microstructures of real face masks on the dynamics, coalescence, and collection of droplets that are comparable in size to the pores (10-40 microns). The mechanisms of transport and capture of such droplets are primarily mechanical interception and then capillary transport, and in this work, we focus on the former. Our simulations will predict the average distance traveled by droplets before being captured and the penetration length that takes place in different layers of a face mask. We primarily focus

here on the role of fiber and pore sizes rather than on the effect of, for example, different wettabilities of fibrous structures. Such a study is a necessary step in formulating guidelines for designing face mask microstructures, where machine learning tools are also to be employed.

Scientific machine learning methods represent a promising tool to model droplet dynamics within the face mask microstructure. A neural operator network such as DeepONet [13] can be used to implement a surrogate model that predicts the droplet invasion time at the microscopic scale of a face mask. The model comprises a trunk network, which encodes the pore microstructure and current invasion state, and a branch network, which processes the water front height and distance from the inlet. Training data are produced via detailed numerical simulations of droplet transport in representative pore geometries, ensuring that the physics of the invasion process is accurately captured. The model outputs a single scalar value representing the invasion time of the central pore, thus offering a refined description of the local dynamics. This surrogate model can then be integrated into a computational fluid dynamics (CFD) simulation, where a simple and numerically efficient interface can represent the mask. The possibility of bridging the scales between the microscopic particle-level description of the droplet dynamics within the pore geometry and the continuum-level description of the airflow through the mask represents the perfect stage for the employment of architectures like neural operators [14, 15]. The efficiency of this approach is particularly useful under realistic respiratory boundary conditions, as it bridges the gap between fine-scale accuracy and large-scale performance for droplet transport analysis.

2.3. Numerical simulations of droplet/air two-phase flow

The transport of saliva droplets has been modeled using the reactingParcelFoam solver from OpenFOAM v21.06 [16]. Turbulence in the continuous phase can be accounted for using either Reynolds-Averaged Navier-Stokes (RANS) or Large Eddy Simulation (LES) models. LPT is employed to track parcels of saliva droplets.

The presence of a face mask must be modeled in both the continuous and discrete phases. In the continuous phase, the face mask induces a pressure drop. Similarly to published literature (see, e.g., [17, 7]), this pressure drop is modeled by introducing a porous region using the Darcy-Forchheimer model, which describes the pressure drop across a porous material of thickness L according to Eq. 1.

$$\Delta p/L = \mu D\underline{u} + 0.5\rho F\underline{u}^2 \tag{1}$$

The model coefficients (D, F) are obtained from the pressure drop measurements reported in [11].

A complicating factor is that the face mask is typically very thin compared to the scales of other geometries that need to be considered. Consequently, adding source terms to impose the required pressure drop may lead to numerical stability issues. Similar numerical challenges arise in combustion modeling, where very thin flame fronts create large temperature gradients.

An approach to handle these gradients without requiring an extremely refined mesh is the so-called thickened flame model (see, e.g., [9]). In this method, the diffusivity coefficient is multiplied by a constant, while the reaction rates are divided by the same constant, effectively thickening the flame front by the same factor while preserving the laminar flame speed. Here, we adopt a similar approach to artificially thicken the face mask zone while maintaining the required pressure drop.

In the computational domain, the face mask is represented with a thickness multiplied by a factor C (see Figure 2). Simultaneously, the coefficients in the Darcy-Forchheimer model are divided by the same factor, ensuring that the imposed pressure drop remains unaffected (see Eq. 1).

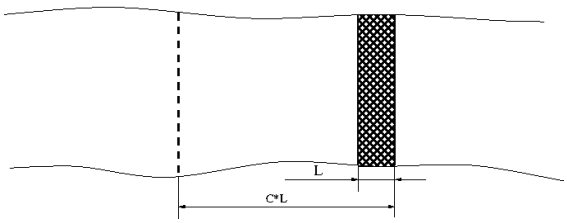

Figure 2. Sketch of the thickened face mask model.

To model the filtration effect of the mask on the discrete phase, two coupled internal boundaries are introduced in the computational domain, corresponding to the two sides of the mask. When a parcel hits one of these boundaries, the number of droplets in the parcel is reduced according to a prescribed filtration efficiency as a function of the droplet diameter. If all droplets are filtered out in the parcel, the parcel is removed. If there are droplets remaining after filtration, the parcel is transferred to the other side of the mask and transported further by the flow.

3. RESULTS

3.1. Droplet dynamics in a face mask microstructure

On the way to formulating a predictive model for droplet interception, we argue that the distance a droplet travels before interception largely depends on the probable size of the pore that the incoming droplet encounters when entering the fibrous medium. Among other things, it is of interest to look at the susceptibility of pores of different sizes to droplet invasion and subsequent collection. In that sense, we differentiate small, medium, and large pores, defined by the relative ratios of a characteristic droplet-to-fiber size ratio to a microstructural parameter of a

mask (defined using porosity of the fibrous medium, the specific surface area, and the fiber diameter). For small pores, which are smaller than droplets, it is straightforward that they will not be easily accessible, given the high capillary pressure required for their invasion. The medium-sized pores are instead more accessible, and should thus allow droplet invasion and collection. These arguments are indeed intuitive, which is not the case for large pores, where we observe a low probability of droplet invasion. Figure 3 shows that only one out of three large pores is invaded. We explain this by the fact that large pores are delimited by a high number of fibers along their perimeter, which significantly reduces the pore-throat size in their proximity. Droplet coalescence also plays a role here, since droplets tend to accumulate at these small pore throats, thus limiting to an even greater extent the access to the large pores.

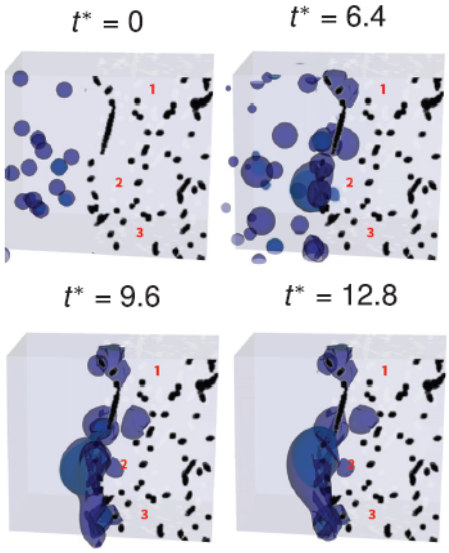

Figure 3. Snapshots of 10–40 micron droplets intercepted in a mask fibrous microstructure obtained by lattice Boltzmann simulations. Large pores are indicated by numbers 1-3, with only pore 2 being invaded.

3.2. Experimental results

Figure 4 shows the droplet distribution after the mask (green triangles), alongside the distribution of the droplets before the mask (blue diamonds) and the filtration efficiency (red rectangles). The droplet distribution before the mask is assumed to match the droplet distribution measured at the outlet when the mask is removed. The results correspond to the cotton cloth and C-19 face masks, both of which exhibited similar filtration efficiency [11]. For better visibility, the droplet size distributions are normalized by the maximum value without a mask.

The droplet size distribution after the face mask is calculated according to Eq. 2, where $\wp(d)$ represents the normalized size distribution of the droplets

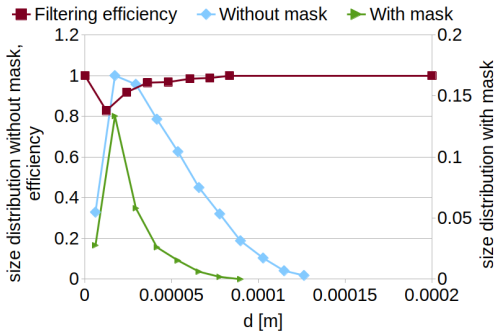

Figure 4. Filtering efficiency and droplet size distributions with and without the face mask.

before the mask at droplet size d, and $\wp_m$ denotes the size distribution of droplets after passing through the face mask. The parameter η represents the filtration efficiency, which is a function of droplet diameter.

$$\wp_m(d) = (1 - \eta(d))\wp(d) \tag{2}$$

The lowest filtration efficiency is approximately 80%, occurring for droplet sizes around 10 μm. Increasing or decreasing the droplet size leads to higher filtration efficiency. When the droplet size exceeds 80 μm, the droplets are completely stopped by the mask. Most droplets emitted at the outlet fall within the size range of 20–50 μm. Ref. [11] gives a more detailed presentation of the results.

3.3. Validation of numerical simulations (LPT)

Figure 5 presents the velocity field and droplet distribution in the branching pipes. The upper figure illustrates the water droplets. The exit of the computational domain is slightly extended to include the flow downstream of the face mask. This facilitates the counting of the leaked droplet numbers and their size distribution. These results align well with the experimental findings discussed in the previous section.

The numerical results provide insight into the droplet dynamics in the branching pipes. First, as shown in the upper sub-figure of Fig. 5, a large number of water droplets adhere to the walls and do not move toward the outlet. Second, the interaction between the droplet-laden flow in the upper branch pipe and the airflow from the lower pipe at the interconnection section creates a recirculating flow. As a result, some droplets move upstream in the lower air pipe and eventually deposit on the walls. Thus, the droplets arriving at the face mask are only a fraction of those injected.

The filtration efficiency obtained from the experimental measurements, shown in Figure 4 as red rectangles, was used in the LES to determine the particle size distribution after the mask. The particle size distribution at the outlet without a face mask was used as the droplet size distribution at the inlet. While

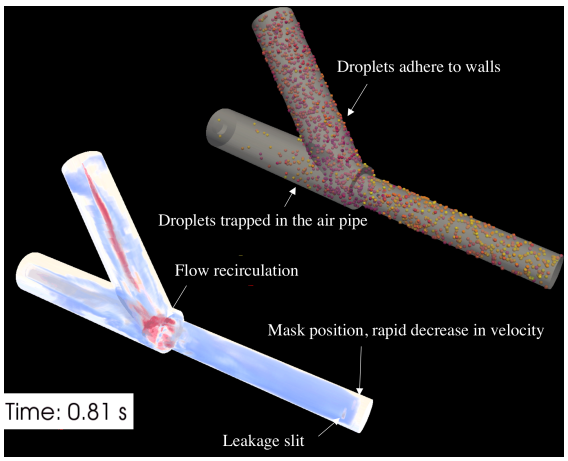

Figure 5. Instantaneous flow velocity and droplet distribution in the pipes.

this provides a qualitatively good approximation of the actual two-phase flow process, a more precise assessment should ideally be based on measurements of droplets directly at the inlet. As seen from the droplet distribution in the branching pipes, a fraction of the droplets is deposited on the walls; thus, the size distribution at the outlet and inlet differ. The particle size distribution near the leakage slit was sampled to validate against the experiments.

3.4. Simulation of flow and droplet distribution during coughing

LES is applied to study droplet distribution during human coughing. The one-equation dynamic k model is used to account for sub-grid scale effects. These computations aim to assess the impact of wearing a mask by comparing two cases: with and without a mask. In both cases, a single coughing event is simulated, with the velocity profile based on the data reported in [18] and plotted in Figure 6.

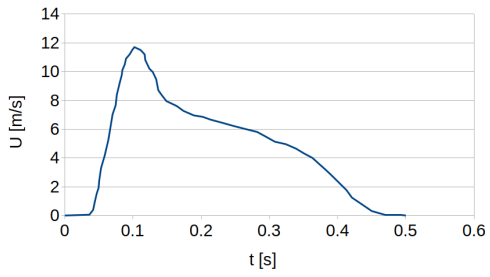

Figure 6. Velocity profile used to simulate a coughing event

A realistic face is included only in the case where the face mask is fitted, as it is important to account for potential leakage in this scenario. Figure 8 illustrates the adopted face geometry, highlighting the placement of the face mask region and the possible leakage areas around the jaw and nose, which are marked with red ellipses. The mouth shape is simplified as a 4×1 cm^2 rectangle. As shown in Fig. 6, a realistic velocity profile is used to mimic the coughing process. The duration of the cough is 0.5 ms, and the maximum velocity is set to 11.7 m/s [19]. The LPT approach is adopted here, and 3000 parcels are used to track the evolution of saliva droplets. The total mass is 7.7 mg, and the droplet size distribution is plotted in Figure 7. Following suggestions in Ref. [20], the size distribution of saliva droplets is initialized using the Rosin-Rammler distribution law. The mean and maximum diameters of 80 and 600 μm are adopted based on measurements in Ref. [21].

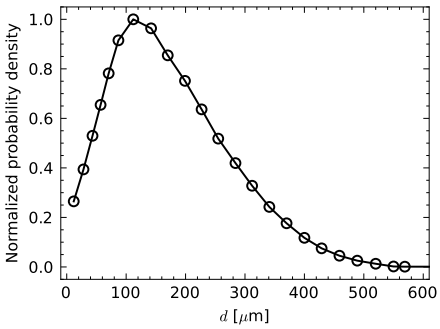

Figure 7. Size distribution of the injected droplets.

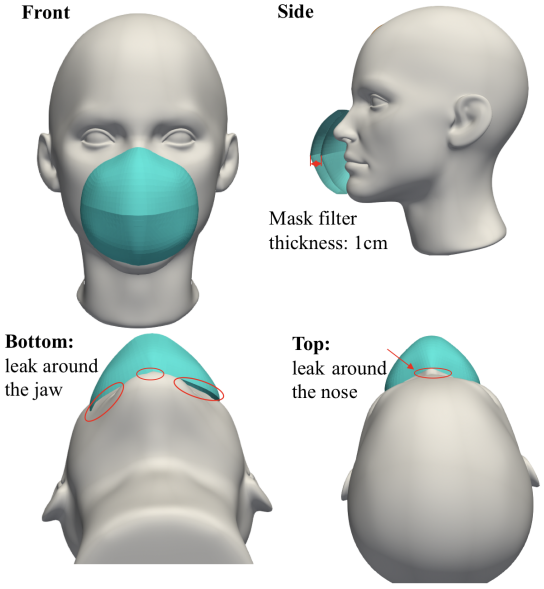

Figure 8. Face model with the mask.

Figure 9 shows the recorded flow rate with and without the face mask. In the numerical simulations, the face mask consists of a set of computational cells, delimited by two patches, i.e., the inner patch and the outer patch. The inner patch is the one close to the inlet, i.e., the mouth, and the outer patch is on the opposite side. The flow rates are calculated as $\sum \rho \underline{u} \cdot \underline{n} A_i$, where $\underline{n}$ and A_i are the normal vector and surface area of the i-th face on the outer patch.

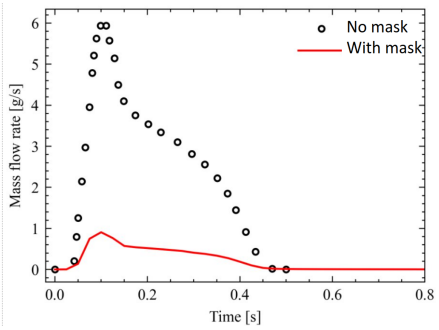

Figure 9. Flowrate with and without mask.

In the case without a face mask, the flow rate is estimated using a virtual patch, i.e., a sampling surface consisting of identical faces to the outer patch. It can be observed that the maximum flow rate is reduced by approximately a factor of six when the face mask is fitted. This factor is slightly lower after 0.15 ms. The flow speed significantly decreases after passing through the face mask due to the pressure loss across it and the leakage of the gas around the nose and jaw. This implies that the leakage cannot be ignored, as it may play an important role in flow fields and the evolution of droplets.

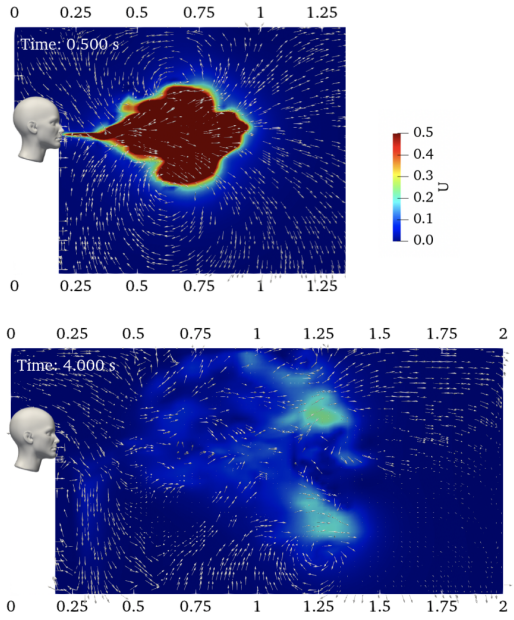

Figure 10. Velocity distribution during human coughing without wearing a face mask.

Figure 10 shows the velocity field at two time instances, i.e., at 0.5 s (top) and 4 s (bottom). The face mask is absent for this case. At 0.5 s, which corresponds to the end of the coughing event, a high-speed flow region with a velocity of approximately 0.5 m/s extends up to 1 m from the human face. By 4 s, the velocity decreases to 0.2 m/s, reaching a distance of 1.5 m. This suggests that a coughing event may affect flow fields at a distance of at least 1.5 meters, consistent with the safety distance.

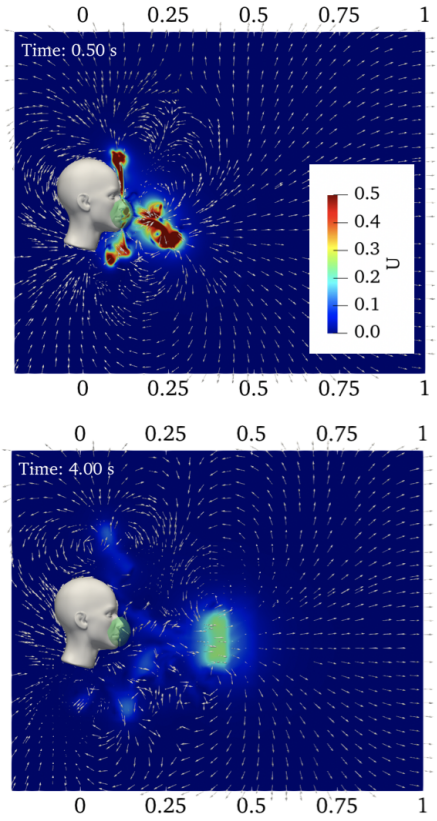

Figure 11. Velocity distribution during human coughing when wearing a face mask.

Figure 11 shows the corresponding velocity field for the case with a face mask. At 0.5 s, three high-speed streams are observed, directed forward, upward, and downward. The upward and downward flow streams result from gaps between the face and the mask around the nose and jaw. This is consistent with observations in Fig. 9, i.e., the penetration of the coughing in the bulk flow direction is reduced, attributed to the mass flow rate of leakage near the nose and jaw.

From Figs. 10 and 11, the impact of the face mask on flow and droplet distribution becomes evident. Due to the significant velocity decrease across the mask, the momentum of droplets moving forward in the horizontal direction is substantially reduced. By 4 s, the velocity of the front stream decreases to approximately 0.2 m/s, reaching only 0.5 m from the face, one-third of the distance observed without the face mask. Additionally, the high filtration efficiency effectively blocks the majority of droplets, thereby reducing the spread of the virus in the air.

3.5. Predicting invasion time with a neural-operator surrogate

As outlined in Sec. 2.2, we employ a DeepONet-style neural operator to predict the invasion time at the pore scale of a facemask. Both subnetworks share a compact, fully connected architecture: Branch net (2 hidden layers, 32 and 16 neurons, respectively), Trunk net (3 hidden layers with 32, 32, and 16 neurons).

All hidden layers use ReLU activation; the latent dimension of each subnetwork is fixed to 32. A single linear neuron in the output layer returns the (scalar) invasion time. The network is trained with Adam and mean–squared error loss; convergence is reached after ≈ 200 epochs.

Model I: absolute time without distance. The first model feeds the pillar diameters (*branch*) and the binary occupation state of the immediate neighbours (*trunk*). Its target is the *absolute* invasion time, measured from $t = 0$ of the simulation. The parity plot in Fig. 12 (top) and the low coefficient of determination ($R^2 = 0.285$) reveal that these inputs are insufficient to capture the invasion dynamics.

Model II: absolute time with distance. To provide a clear physical proxy for front progression, we append the absolute distance from the mask edge to the trunk input. As expected, the network now attains excellent accuracy ($R^2 = 0.989$; Fig. 12 middle), essentially learning the monotonic relationship between distance and arrival time of the wetting front.

Model III: relative time without distance. Finally, we withdraw the distance feature and ask the network to predict the *relative* invasion time, defined as the time elapsed since one of the adjacent pores was first invaded. Although trained on the same data volume as the previous models, Model III already achieves a promising $R^2 = 0.825$ (Fig. 12, bottom). This indicates that local geometry and short-range state information are sufficient to reconstruct the temporal ordering of pore invasion, provided a larger training set.

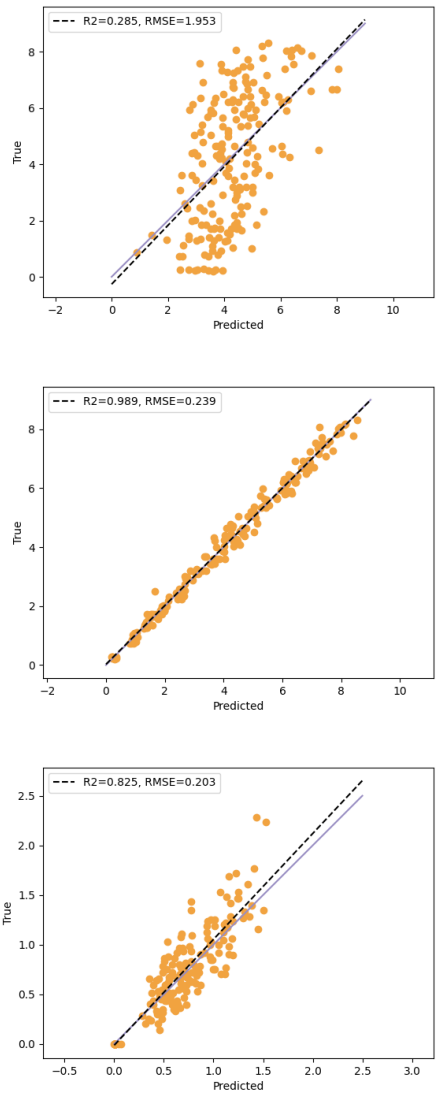

Figure 12. Parity plots for Model I (top), II (middle) and III (bottom). The dashed line is $y = x$.

4. SUMMARY

This paper presents experimental and numerical studies on the filtration of liquid droplets through face masks. Experimental investigations were conducted using a branching pipe rig to analyze water droplet filtration across various face masks, measuring particle size distributions at the outlet with and without masks. The results showed that droplets larger than 80 μm were effectively filtered out, while the lowest filtration efficiency, approximately 80%, was observed for droplets around 10 μm in diameter.

Lattice Boltzmann simulations of droplet interception and collection in the mask revealed that, counterintuitively, not all large pores are penetrated by droplets.

The analysis based on the neural operator revealed that, with additional data, a distance-free surrogate could faithfully reproduce pore-scale invasion dynamics. This represents an essential step toward embedding pore physics in continuum-scale CFD simulations.

A thickened mask model was developed within the large eddy simulation (LES) framework to simulate droplet/air two-phase flow across the mask. Numerical simulations using this model were performed to study droplet and turbulent flow behavior within the branching pipe rig. The results provided insights into droplet motion, wall deposition, recirculating flow, and the rapid velocity drop across the mask.

The thickened mask model was further applied to simulate airflow during human coughing, both with and without a face mask. The results revealed a significantly reduced penetration distance of the forward flow and detailed the airflow structure through gaps between the mask and the nose and jaw. Future work will focus on using the model to optimize the

design of reusable face masks.

ACKNOWLEDGEMENTS

This work was supported by Formas (Project number 2022-01116). The computations were enabled by resources provided by NAISS at NSC and PDC, partially funded by the Swedish Research Council through grant agreement no. 2022-06725 and no. 2018-05973.

REFERENCES

[1] Prata, J. C., Silva, A. L., Walker, T. R., Duarte, A. C., and Rocha-Santos, T., 2020, "COVID-19 pandemic repercussions on the use and management of plastics", *Environmental science & technology*, Vol. 54 (13), pp. 7760–7765.

[2] Corburn, J., Vlahov, D., et al., 2020, "Slum health: arresting COVID-19 and improving well-being in urban informal settlements", *Journal of urban health*, Vol. 97, pp. 348–357.

[3] WHO, "Coronavirus Disease (COVID-19) Advice for the Public: When and How to Use Masks", URL `https://www.who.int/emergencies/diseases/novel-coronavirus-2019/advice-for-public/when-and-how-to-use-masks`, checked 2025.03.06.

[4] Silva, A. L., Prata, J. C., Duarte, A. C., Soares, A. M., Barceló, D., and Rocha-Santos, T., 2021, "Microplastics in landfill leachates: The need for reconnaissance studies and remediation technologies", *Case Studies in Chemical and Environmental Engineering*, Vol. 3, p. 100072.

[5] Jain, S., Yadav Lamba, B., Kumar, S., and Singh, D., 2022, "Strategy for repurposing of disposed PPE kits by production of biofuel: Pressing priority amidst COVID-19 pandemic", *Biofuels*, Vol. 13 (5), pp. 545–549.

[6] Klemeš, J. J., Van Fan, Y., and Jiang, P., 2020, "The energy and environmental footprints of COVID-19 fighting measures–PPE, disinfection, supply chains", *Energy*, Vol. 211, p. 118701.

[7] Mittal, R., Breuer, K., and Seo, J. H., 2023, "The Flow Physics of Face Masks", *Annual Review of Fluid Mechanics*, Vol. 55 (1), pp. 193–211.

[8] Hu, N., Yuan, F., Gram, A., Yao, R., and Sadrizadeh, S., 2024, "Review of experimental measurements on particle size distribution and airflow behaviors during human respiration", *Building and Environment*, Vol. 247 (October 2023), p. 110994.

[9] Detomaso, N., Hok, J.-J., Dounia, O., Laera, D., and Poinsot, T., 2023, "A generalization of the Thickened Flame model for stretched flames", *Combustion and Flame*, Vol. 258, p. 113080.

[10] Semidetnov, N., and Tropea, C., 2003, "Conversion relationships for multidimensional particle sizing techniques", *Measurement Science and Technology*, Vol. 15 (1), p. 112.

[11] Öhman, J., Gren, P., Sjödahl, M., and Lundström, T. S., 2022, "Experimental investigation of face mask filtration in the 15-150 μm range for stationary flows", *Journal of Applied Physics*, Vol. 131, p. 044702.

[12] Öhman, J., and Sjödahl, M., 2020, "Identification, tracking, and sizing of nano-sized particles using dual-view polarization-resolved digital holography and T-matrix modeling", *Applied Optics*, Vol. 59 (14), pp. 4548–4556.

[13] Lu, L., Jin, P., Pang, G., Zhang, Z., and Karniadakis, G. E., 2021, "Learning nonlinear operators via DeepONet based on the universal approximation theorem of operators", *Nature machine intelligence*, Vol. 3 (3), pp. 218–229.

[14] Laudato, M., Manzari, L., and Shukla, K., 2024, "High-Fidelity Description of Platelet Deformation Using a Neural Operator", *arXiv preprint arXiv:241200747*.

[15] Laudato, M., Manzari, L., and Shukla, K., 2025, "Neural Operator Modeling of Platelet Geometry and Stress in Shear Flow", *arXiv preprint arXiv:250312074*.

[16] OpenFOAM, "OpenFOAM, https://www.openfoam.com", Checked 2025.02.18.

[17] Jia, Z., Ai, Z., Yang, X., Mak, C. M., and Wong, H. M., 2023, "Towards an accurate CFD prediction of airflow and dispersion through face mask", *Building and Environment*, Vol. 229 (November 2022), p. 109932.

[18] Gupta, J. K., Lin, C. H., and Chen, Q., 2009, "Flow dynamics and characterization of a cough", *Indoor Air*, Vol. 19 (6), pp. 517–525.

[19] Gupta, J. K., Lin, C.-H., and Chen, Q., 2009, "Flow dynamics and characterization of a cough", *Indoor air*, Vol. 19 (6), pp. 517–525.

[20] Dbouk, T., and Drikakis, D., 2020, "On coughing and airborne droplet transmission to humans", *Physics of Fluids*, Vol. 32 (5).

[21] Xie, X., Li, Y., Sun, H., and Liu, L., 2009, "Exhaled droplets due to talking and coughing", *Journal of the Royal Society Interface*, Vol. 6 (suppl_6), pp. S703–S714.